Contents lists available at ScienceDirect

Progress in Natural Science: Materials International

journal homepage: www.elsevier.com/locate/pnsmi

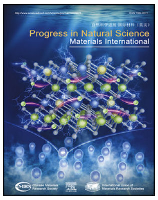

Ultrafast joule-heating synthesis of FeCoMnCuAl high-entropy-alloy nanoparticles as efficient OER electrocatalysts

Xindong Zhu[a,1], Wen Huang[a,1], Yu Lou[a], Zhongzheng Yao[a], Huiqiang Ying[a], Min Dong[a], Lan Tan[a], Jianrong Zeng[b,c], Hua Ji[d,e,**], He Zhu[a,*], Si Lan[a,***]

[a] Herbert Gleiter Institute of Nanoscience, School of Materials Science and Engineering, Nanjing University of Science and Technology, Nanjing, 210094, China
[b] Shanghai Synchrotron Radiation Facility, Shanghai Advanced Research Institute, Chinese Academy of Sciences, Shanghai, 201204, China
[c] Shanghai Institute of Applied Physics, Chinese Academy of Sciences, Shanghai, 201800, China
[d] Scientific Research and Innovation Center, Suzhou Nuclear Power Research Institute, Suzhou, 215004, China
[e] National Engineering Research Center for Nuclear Power Plant Safety & Reliability, Suzhou, 215004, China

ABSTRACT

High entropy alloys (HEAs), known for their synergistic orbital interactions among multiple elements, have been recognized as promising electrocatalysts for enhancing the sluggish kinetics of oxygen evolution reaction (OER). Despite their potential, the facile and rapid preparation of HEA nanoparticles (NPs) with high electrocatalytic activity remains challenging. Here, we report an ultrafast synthesis of noble-metal-free FeCoMnCuAl HEA NPs loaded on conductive carbon fiber networks using a Joule heating strategy. The prepared HEA NPs exhibited a face-centered cubic (FCC) structure with an average size of approximately 25 nm. Synchrotron X-ray absorption fine structure (XAFS) and X-ray photoelectron spectroscopy (XPS) studies were performed to investigate the atomic and electronic structures of the HEA NPs, revealing the co-presence of Fe, Co, Mn, Cu and Al elements as well as their different valences across surface and internal regions. The HEA NPs showed remarkable OER performance, exhibiting an overpotential of 280 mV at 10 mA cm^{-2} and a low Tafel slope of 76.13 mV dec^{-1} in a 1.0 M KOH solution with high electrochemical stability, superior to commercial RuO_2 electrocatalysts. This work provides a new approach for synthesizing nanoscale noble-metal-free HEA electrocatalysts for clean energy conversion applications on a large-scale basis for practical commercialization.

1. Introduction

Due to the increasing consumption of fossil fuels and the ever-rising environmental pollution, the demand for sustainable and green energy sources has become increasingly critical. Among the potential solutions, the electrocatalytic splitting of water has gained significant attention as a promising and cost-effective technology for clean energy conversion over the past few decades [1–5]. The oxygen evolution reaction (OER) is an indispensable half reaction in this process, necessary for producing hydrogen energy through water splitting [6–8]. However, the OER involves a complex four-electron transfer mechanism, resulting in sluggish kinetics and a large overpotential to achieve the desired current density [9]. Currently, commercial OER electrocatalysts primarily rely on noble metals such as Ru and Ir [10–12]. Despite their high activity, the widespread applications of these electrocatalysts are severely hindered by their high costs, scarcity, and instability under operational conditions [13]. Therefore, there is an urgent need to develop efficient, durable, and low-cost non-noble-metal-based electrocatalysts with satisfactory OER performance [14–18].

High entropy alloy (HEA) is an alloy composed of five or more elements in nearly equal atomic ratios, with each element content ranging from 5 % to 35 % (at.%) [19,20]. The unique multi-element configuration of HEAs allows for the overlapping of orbitals, forming numerous bonding and, in particular, antibonding orbitals with high-energy electrons occupied [21–23]. The adsorption capability of active sites is thus optimized, thereby improving their electrocatalytic activities [24–26]. Moreover, the size differences between various atoms in HEAs drive them to shift from ideal lattice positions. The resultant lattice distortion increases the exposure of active sites (*e.g.*, surface defects) [27] and optimizes the electronic structures of active sites [28–30], eventually improving electrocatalytic performance. These advantages enable HEAs, particularly those incorporating earth-abundant 3*d* transition elements like Fe, Co, Mn and Cu, to exhibit OER activity comparable to that of noble 4*d* or 5*d* metals [31–36]. Nevertheless, challenges lie in the

---

* Corresponding author.
** Corresponding author. Scientific Research and Innovation Center, Suzhou Nuclear Power Research Institute, Suzhou, 215004, China.
*** Corresponding author.
E-mail addresses: jihuanust@163.com (H. Ji), hezhu@njust.edu.cn (H. Zhu), lansi@njust.edu.cn (S. Lan).

[1] These authors contributed equally: Xindong Zhu, Wen Huang.

https://doi.org/10.1016/j.pnsc.2024.08.005
Received 12 June 2024; Received in revised form 5 August 2024; Accepted 17 August 2024

Please cite this article as: X. Zhu et al., Ultrafast joule-heating synthesis of FeCoMnCuAl high-entropy-alloy nanoparticles as efficient OER electrocatalysts, Progress in Natural Science: Materials International, https://doi.org/10.1016/j.pnsc.2024.08.005

preparation of nanosized HEAs with high specific surface areas and uniform elemental distributions. Additionally, tunning the synergistic effects through the selection of appropriate elemental combinations is crucial to maximizing their OER activities.

High-temperature shock (HTS) method has been recently proposed as a promising technique for preparing metastable nanomaterials, including nano HEAs [37–41]. This method uses the Joule heating principle, where electrical energy is rapidly converted into thermal energy as current flows through carbon fibers. In this way, a rapid heating and cooling process is enabled, reaching temperatures up to 2000 K and then cooling to room temperature within a few milliseconds. In contrast to traditional methods where prolonged heating and cooling periods lead to crystal growth, the HTS method can effectively suppress phase separation, atomic diffusion, and particle aggregation during synthesis through its ultrafast heating and cooling rates. The non-equilibrium kinetic process is triggered under the extreme conditions of HTS method, facilitating the formation of evenly distributed ultrafine metastable HEA nanocrystals. Defects such as vacancies, dislocations, and strains are effectively maintained within these metastable nanostructures, generating abundant catalytic active sites [42,43]. Meanwhile, the high-density defects are also generated on the carbon-fiber substrate, which can effectively disperse the NPs that may agglomerate during conventional heat treatment, thereby benefitting the synthesis of ultrafine HEA NPs [44,45]. However, further validation of the HTS method in the field of HEA electrocatalyst is still highly desired to fully establish its potential and applicability.

In this work, we present the synthesis of FeCoMnCuAl HEA NPs deposited on treated carbon cloth *via* a rapid HTS method, demonstrating superior electrocatalytic OER performance. During this HTS process, surface defects form on the carbon substrate, which facilitates uniform dispersion of the NPs. The resulting HEA NPs exhibit a FCC single phase taking advantage of the ultrahigh-rate HTS process. Synchrotron X-ray pair distribution function (PDF) and X-ray absorption fine structure (XAFS) analyses reveal detailed insights into the atomic and electronic structures of the HEA NPs. Comprehensive electrochemical tests reveal that the FeCoMnCuAl HEA NPs exhibit high OER performance superior than commercial RuO_2 electrocatalyst. The proposed HTS strategy for preparing noble-metal-free HEA NPs paves the way for the development of cutting-edge electrocatalytic materials.

2. Materials and methods

2.1. Materials

Ferric chloride hexahydrate ($FeCl_3 \cdot 6H_2O$, 99.1 %), cobalt chloride hexahydrate ($CoCl_2 \cdot 6H_2O$, AR), manganese chloride tetrahydrate ($MnCl_2 \cdot 4H_2O$, 99 %), copper chloride dihydrate ($CuCl_2 \cdot 2H_2O$, 99 %), and aluminum chloride hexahydrate ($AlCl_3 \cdot 6H_2O$, AR) were purchased from Chinese Sinopharm Chemical Reagent Co., Ltd. (Shanghai, China). Acetone (AR), oxalate (99 %), and ethanol (99.5 %) were purchased from MACKLIN. Commercial RuO_2 were purchased from Taiwan Carbon Energy Technology Co., Ltd. Carbon cloth and carbon felt were purchased from Aladdin Industrial Corporation (Shanghai, China).

2.2. Preparation of FeCoMnCuAl

First, the carbon cloth underwent a pre-treatment process involving ultrasonic cleaning in acetone, ethanol and deionized water for 30 min, followed by drying in a 60 °C oven. The pre-treated carbon cloths were further treated by three different methods and denoted as A-cc, H-cc, and AH-cc, respectively. A-cc was obtained by ultrasonically soaking the carbon cloth in saturated oxalic acid solution for 1 h, then washed and dried in a 60 °C oven. H-cc was obtained after exposing the carbon cloth to CO_2 at 850 °C for 2 h. AH-cc was obtained by heating the carbon cloth under CO_2 atmosphere after acid foaming treatment. Next, the carbon cloths from these treatments were soaked in the precursor solution. This solution was prepared by dissolving equal molar ratios of $FeCl_3 \cdot 6H_2O$, $CoCl_2 \cdot 6H_2O$, $MnCl_2 \cdot 4H_2O$, $CuCl_2 \cdot 2H_2O$ and $AlCl_3 \cdot 6H_2O$ in ethanol. The pre-treated carbon cloth was then immersed in this precursor solution and pressed to ensure thorough soaking for 5 min. After soaking, the carbon cloth was dried in an oven at 60 °C. Finally, FeCoMnCuAl HEA NPs were synthesized on the carbon cloth using the HTS method. A carbon felt was clamped on both sides of a copper sample stage, with the carbon cloth placed on top. The synthesis was carried out with a current of 90 A and a voltage of 32 V, achieving a maximum temperature of 1500 °C under an argon atmosphere.

2.3. Material characterization

X-ray diffraction (XRD, Bruker-AXS D8 Advance) was used to determine the crystal structure of the HEA NPs. The morphology and microstructure of the as-prepared HEA NPs was examined by a scanning electron microscope (SEM, JSM-7800F PRIME) operated at 5 kV and a transmission electron microscopy (TEM, JEOL JEM-2100F) operated at 200 kV. Elemental composition was determined using energy dispersive spectrum (EDS, X-Max 80) and inductively coupled plasma mass spectrometry (ICP-MS). X-ray photoelectron spectroscopy (XPS, ESCALAB 250Xi) with an Al-Kα radiation source (1486.6 eV) was used to analyze the valence states of the elements on the HEA NP surfaces, with binding energy calibrated against the C 1*s* peak at 284 eV. Raman spectroscopy (HR EVO NANO) with a 532 nm laser source was used to study the structural changes of the pristine and pre-treated carbon cloth.

Synchrotron X-ray total scattering measurements were performed at the BL13SSW beamline of the Shanghai Synchrotron Radiation Facility (SSRF [46]). The center energy of the radiated X-rays was 50.00 keV, corresponding to a wavelength $\lambda = 0.2480$ Å. The PDF was obtained from the raw total scattering data after corrections for environmental scattering, incoherent and multiple scattering, polarization and absorption using PDFgetX2 software with $Q_{max} = 16.0$ Å^{-1} [47]. The X-ray absorption fine structure (XAFS) measurements were also collected at the BL13SSW of the SSRF. The X-ray absorption near-edge structure (XANES) and extended X-ray absorption fine structure (EXAFS) were processed using ATHENA software [48].

2.4. Electrochemical test

Electrochemical measurements were conducted in a three-electrode electrochemical cell using Pt sheets as the counter electrode and Ag/AgCl as the reference electrodes. The electrolyte as a 1 M KOH solution (pH = 13.6). The reference electrode potential was converted to the RHE scale using the equation: E (RHE) = E (Ag/AgCl) + 0.197 V + 0.0592 × pH. The linear sweep voltammetry (LSV) was tested from 1.2 V to 1.8 V (*vs* RHE) at a scan rate of 10 mV s^{-1} with a 100 % IR compensation after the working electrodes were activated for several times until stable signals were achieved. The electrochemical double-layer capacitance (C_{dl}) was determined by cyclic voltammetry (CV) in the non-Faradaic region (0.02–0.12 V *vs* reference electrode) at scan rates of 20, 40, 60, 80, 100, 120 mV s^{-1}, which was utilized to estimate the electrochemically active surface area (ECSA). Electrochemical impedance spectroscopy (EIS) was recorded at 1.5 V (*vs* RHE) over a frequency range from 100000 to 0.1 Hz with a 5 mV AC amplitude.

3. Results and discussion

3.1. Synthesis and characterization of FeCoMnCuAl HEA electrocatalysts

The temperature profile of a typical HTS process at 1400 °C and heating/cooling rate of ~1000 °C per second is shown in Fig. 1(a), and the insets illustrate the setup and critical stages for the synthesis of HEA-NPs supported on carbon cloth. Fig. 1(b) reveals noticeable differences in the Raman spectra of the carbon cloth before and after carbon cloth treatment. The peak D at 1300 cm^{-1} indicates structural defects in the

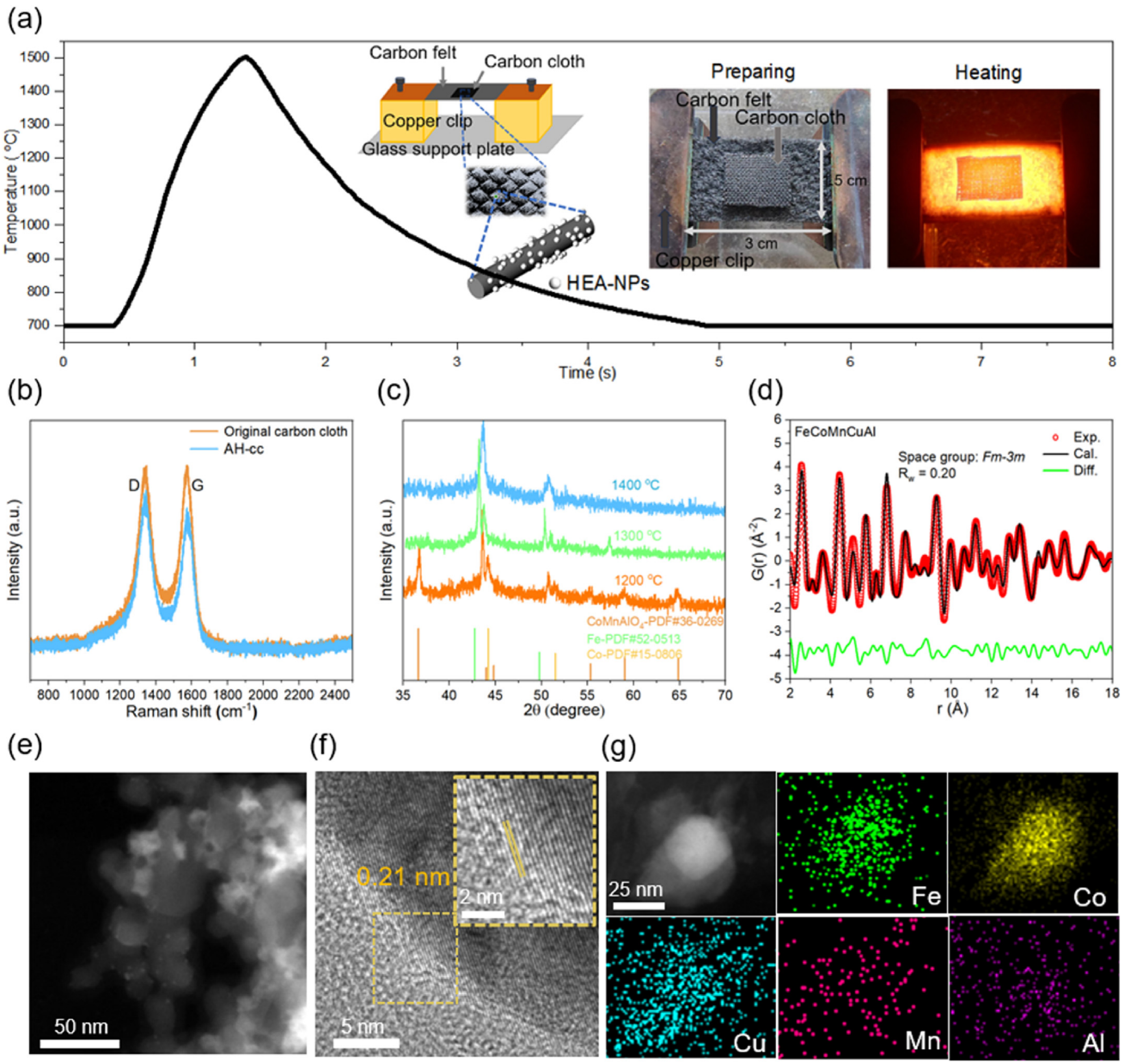

Fig. 1. (a) Temperature profile of a typical HTS synthesis. Insets from left to right are a schematic diagram of the FeCoMnCuAl HEA electrocatalyst, a photograph of preparation, and heating periods of the sample stage. (b) Raman spectra of the original carbon cloth and AH-cc. (c) XRD patterns of the FeCoMnCuAl HEA electrocatalyst prepared at different synthesis temperatures. (d) PDF patterns of the FeCoMnCuAl HEA electrocatalyst. (e) TEM and (f) HRTEM images of FeCoMnCuAl HEA NPs. (g) Elemental mapping of Fe, Co, Mn, Cu, and Al for FeCoMnCuAl HEA NPs.

carbon lattice of six-membered rings, while the peak G at 1580 cm^{-1} corresponds to the in-plane stretching vibration of *sp*^{2}-hybridizd carbon atoms [49–51]. The intensity ratio of the two peaks (ID/IG) represents the degree of defects within the carbon material [52]. The ID/IG ratios of the carbon cloth before and after treatment are 0.99 and 1.18, respectively. The increase in the ID/IG indicates a higher defect content, which enhances the loading capability and uniform dispersion of HEA NPs during the HTS process [53].

XRD measurements were employed to determine the crystal structure of the electrocatalysts. Fig. 1(c) shows the XRD patterns of the electrocatalyst obtained at different temperatures. At a relatively lower temperature of 1200 °C, the as-prepared material exhibited a hybrid phase containing two FCC phases and a phase identical to $CuMnAlO_4$ (PDF#36–0269). As the synthesis temperature increased, the $CuMnAlO_4$ phase disappeared but two FCC phases could be observed. At 1400 °C, a single-phase FeCoMnCuAl HEA material was formed, as evidenced by diffraction peaks at 44.1° and 51.4°, corresponding to the (1 1 1), and (2 0 0) planes of the *Fm-3m* FCC structure. The unit cell parameter *a*, calculated using Bragg formula, was ~3.56 Å. The absence of additional diffraction peaks confirms the formation of a single-phase HEA. Full-profile refinement of synchrotron X-ray PDF was performed to examine the FCC nature of the HEA NPs (Fig. 1(d)). The first peak of the pattern, corresponding to the nearest atomic distance from faced-centered M to corner M (where M represents Fe, Co, Mn, Cu or Al), is located at 2.55 Å in real space. The second peak, representing the length of *a* in the cubic cell, is fitted to be 3.60 Å. This fitted *a* value is slightly larger the XRD results, indicating that there could be some degree of lattice distortion in the local structure of HEA NPs.

The morphology of the HEA NPs was initially analyzed by SEM. As shown in Fig. S1(a), the FeCoMnCuAl synthesized on A-cc (see Methods for the abbreviations of A-, H- and AH-cc) exhibited large, agglomerated NPs with uneven distribution on the carbon cloth surface. Fig. S1(b) shows the FeCoMnCuAl synthesized on H-cc, where the NPs were sparse and large, forming spherical shapes on the carbon cloth. In contrast, Fig. S2 demonstrates that the FeCoMnCuAl synthesized on AH-cc exhibited well-segregated, evenly dispersed spherical NPs with more uniform particle dimensions and higher specific surface area. The improved dispersion of the AH-cc loaded NPs could be attributed to the combined effects of surface modification and heating process during the carbon pre-treatment. Soaking in saturated oxalic acid solution (A-cc) removed most hydrophilic and hydrophobic molecules on the carbon cloth surface, generating more adsorption sites [54]. The H-cc treatment involved high-temperature heating under CO_2 atmosphere, where a $CO_2+C{=}CO$ reaction took place at 850 °C. This process affected carbon cloth surface for generating more surface defects [55]. For AH-cc, the heat treatment generated more surface defects, while the acid treatment increases the number of adsorption sites. These effects improve the dispersion and electrochemical activity of the HEA NPs. As depicted in Fig. S2(b), the majority of nanoparticles are smaller than 100 nm and contribute significantly to catalysis. Particle size analysis of 1000 particles revealed that most FeCoMnCuAl nanoparticles ranged between 20 and 30 nm, with a relatively uniform size distribution (±12 nm). Additionally, EDS mapping of FeCoMnCuAl NPs shows that Fe, Co, Mn, Cu, and Al elements are evenly distributed on the carbon cloth. The much lower signal intensity of Mn may be attributed to its higher vapor pressure, giving rise to a lower concentration of Mn during the HTS process.

TEM images confirm that the FeCoMnCuAl NPs have an average size of ~25 nm (Fig. 1(g)). High-resolution TEM (HRTEM) images (Fig. 1(f)) probed lattice fringes with a spacing of 0.21 nm, corresponding to the (111) plane of the HEA-NPs. This further validates the FCC crystal crystal structure of the prepared FeCoMnCuAl NPs, which is consistent with the XRD and PDF results. TEM-EDS mapping demonstrates a homogeneous distribution of Fe, Co, Mn, Cu, and Al within the NPs, indicating the formation of HEA NPs with uniform composition. Based on ICP-MS results, the FeCoMnCuAl NPs consist of 20 at% Fe, 34 at% Co, 8 at% Mn, 27 at% Cu, and 12 at% Al, consistent with the EDS results shown in Fig. S2(d).

The elemental valence states of the FeCoMnCuAl electrocatalyst were studied by XPS. The full-profile survey scan confirms the presence of Fe, Co, Mn, Cu and Al elements in the HEA NPs (Fig. 2(a)). From the Fe 2*p* spectrum (Fig. 2(b)), the peaks corresponding to Fe^0 and $Fe^{2+/3+}$ were observed. Meanwhile, the Co^0, Co^{2+} and Co^{3+} could be also observed in the Co 2*p* spectrum (Fig. 2(c)). Similarly, the Mn 2*p* spectrum (Fig. 2(d)) shows peaks at 640 eV, 640.9 eV, and 642.1 eV, attributed to Mn^0, Mn^{2+} and Mn^{3+}, respectively. For Cu 2*p* spectrum (Fig. 2(e)), both Cu^{2+} and Cu^0 could be determined. The partial oxidation of electrochemical-active transition metals (i.e., Fe, Co, Ni and Cu) on the HEA surface is believed to enhance adsorption and improve electrochemical activity [56,57]. It has been well recognized that the high-valence transition metals on the surface show strong hydrolysis effect to promote the formation of MOOH, which is an intermediate of the OER reaction that accelerates the electrochemical kinetics. In addition, the partial oxidation of the 3*d* transition metals also induce surface reconstruction and defects, which is also beneficial for the OER reaction [58].

Remarkably, the Al 2*p* spectrum only shows peaks at 76.6 and 74.2 eV, corresponding to the Al^{3+}core levels of $2p_{3/2}$ and $2p_{1/2}$, indicating

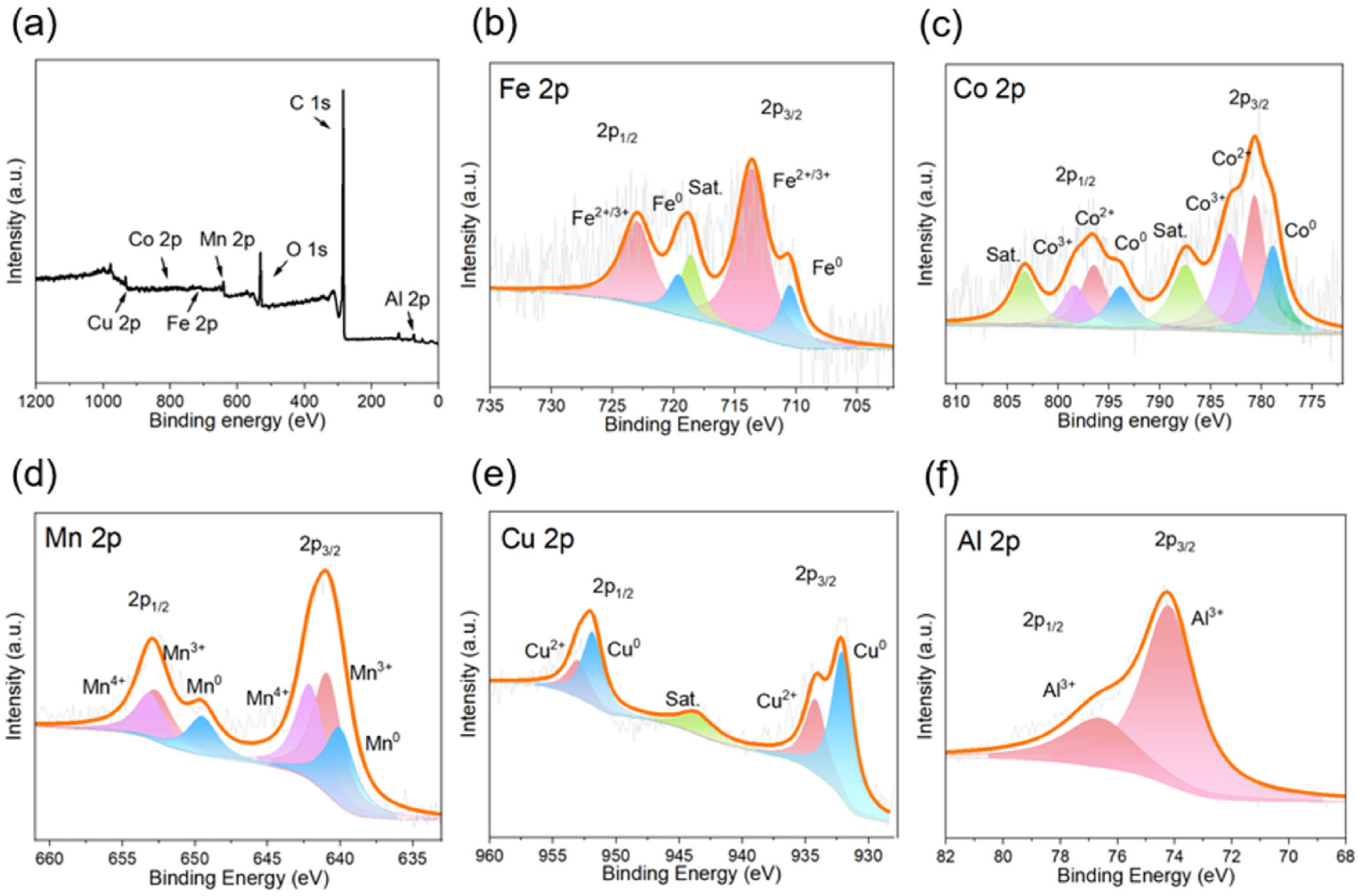

Fig. 2. (a) XPS survey spectrum of the FeCoMnCuAl electrocatalyst. (b–f) Fine scan of XPS spectra showing Fe 2*p*, Co 2*p*, Mn 2*p*, Cu 2*p* and Al 2*p* core levels.

that the surface Al is fully oxidized. This complete oxidation of Al on the surface of electrocatalyst may be beneficial for electrocatalytic performance. It is known that the OER reaction involves four key steps: adsorption of hydroxyl groups, electron-loss oxidation, proton coupling, and electron transfer [59,60]. Typically, Al^0 strongly adsorbs hydroxyl (OH) groups, which can inhibit further electron-loss oxidation and block the OER reactions. The complete passivation of surface Al in our HEA NPs prevents this inhibition [61,62]. Moreover, Al has a good affinity toward O and the formation of Al-O allows the reaction to straightly enter the proton coupling step. This reduces the energy barrier required for the reaction, hence improving the OER performance [63]. In summary, the high-valence states of Fe, Co, Mn, Cu, and Al in the surface region of HEA NPs indicate the inevitable surface oxidation, which may be beneficial to the subsequent OER tests.

XANES analyses were further employed to reveal the oxidation states of various elements in both FeCoMnCuAl and FeCoMnCu electrocatalysts, as shown in Fig. 3(a–d). Compared with the FeCoMnCu electrocatalyst, the Fe, Cu and Mn K-edges in the FeCoMnCuAl slightly shifted to lower energy, indicating a reduction in their valence states. The Co K-edges in the FeCoMnCuAl did not shift to lower energy, indicating that the introduction of Al did not affect the valence states of Co. The XANES results reveal that the introduction of Al can prevent the oxidation of internal elements in the NPs, likely due to the protection effect of surface passivation of Al on the surface of HEA NPs.

3.2. OER performance of the HEA electrocatalyst

The OER performance of FeCoMnCuAl and FeCoMnCu electrocatalysts was evaluated using linear sweep voltammetry (LSV), as shown in Fig. 4(a). At a current density of 10 mA cm^{-2}, FeCoMnCuAl exhibits high OER activity with an overpotential (η_{10}) of ~280 mV, compared to RuO_2 ($\eta_{10} = 295$ mV) and FeCoMnCu ($\eta_{10} = 350$ mV). This highlights the significant enhancement in electrochemical activity attributed to the introduction of Al element. The performance of the carbon cloth substrate alone is negligible (Fig. S3(a)). The Tafel slope, derived from the LSV curve, serves as an important parameter for evaluating reaction kinetics. As shown in Fig. 4(b), the Tafel slope of the FeCoMnCuAl is 76.13 mV·dec^{-1}, which is lower than that of RuO_2 (99.74 mV dec^{-1}) and FeCoMnCu (106.97 mV dec^{-1}). Figs. S3(b–c) shows the LSV curves and Tafel slopes of FeCoMnCuAl synthesized on different carbon substrates, revealing that FeCoMnCuAl loaded on AH-cc shows the best OER performance compared to those loaded on cc, A-cc, and H-cc. To further examine the intrinsic OER activity of the electrocatalysts, the electrochemical active surface area (ECSA) was determined. According to the equation ECSA = C_{dl}/C_s, the ECSA can be estimated using the double-layer capacitance (C_{dl}), where C_s is typically 0.04 mF cm^{-2}. The C_{dl} was calculated by slope of plotting the current density difference as a function of the scanning rate (Fig. S4). The ECSA values for FeCoMnCuAl and FeCoMnCu are 368 cm^2 and 298 cm^2, respectively (Fig. 4(c)). The larger C_{dl} of FeCoMnCuAl indicates a greater number of active sites to accelerate the OER reaction. Furthermore, the electrochemical impedance spectroscopy (EIS) was employed to evaluate the electron transfer kinetics during the OER process, as shown in Fig. 4(d). The smaller semicircle in the high-frequency range for FeCoMnCuAl, compared to FeCoMnCu, indicates a lower charge transfer resistance (R_{ct}), which facilitates the electron transfer and promotes the OER reaction. Fig. 4(e) shows excellent stability of FeCoMnCuAl in alkaline solutions with a current density of 10 mA cm^{-2}, maintaining a long-term stability over a 12-h continuous electrolysis. This stability is notably better than that of the commercial RuO_2, which shows significant performance degradation under similar conditions. Fig. 4(f) shows the LSV curves of the FeCoMnCuAl before and after 1000 cycles in the range of 0.2–0.7 V. The LSV curves are consistent, further demonstrating the excellent electrocatalytic stability of the FeCoMnCuAl.

3.3. Mechanistic insights

In transition metal elements, the electronegativity differences of Fe-Co, Co-Cu, and Cu-Mn are relatively small, with similar valences and small differences in atomic sizes. Upon the addition of Al element, the size mismatch between elements causes lattice distortion, resulting in large diffusion energy barriers and avoiding phase separation. The XRD results shown in Fig. 5(a) indicate that without Al, Cu (PDF#85–1326) component in the FeCoMnCu exhibit significant separation. However,

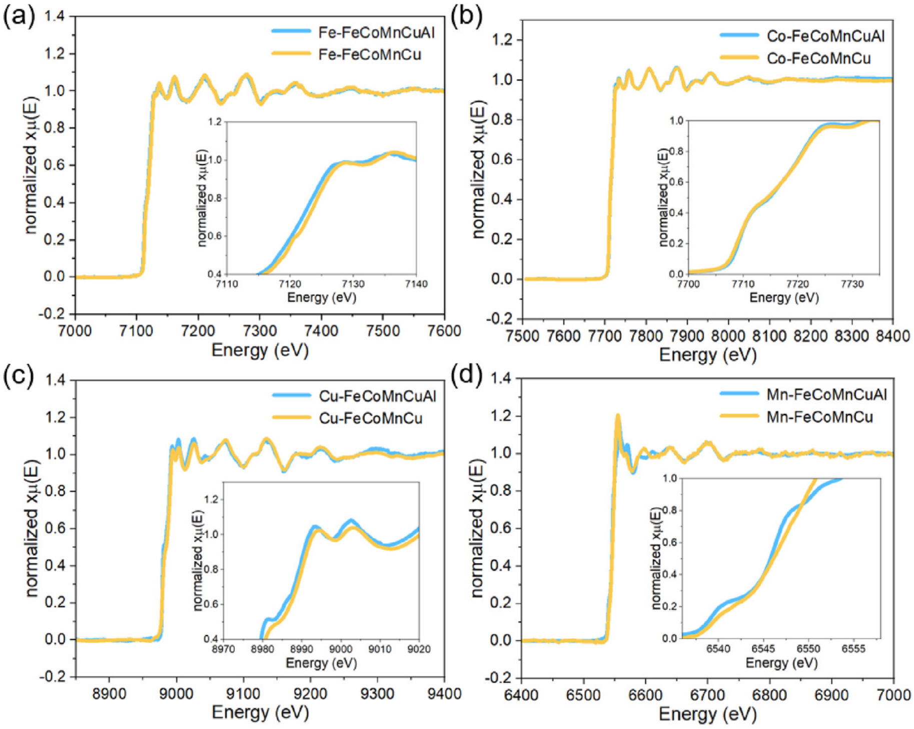

Fig. 3. XANES spectra for (a) Fe K-edge, (b) Co K-edge, (c) Cu K-edge, and (d) Mn K-edge for the FeCoMnCu and FeCoMnCuAl electrocatalysts.

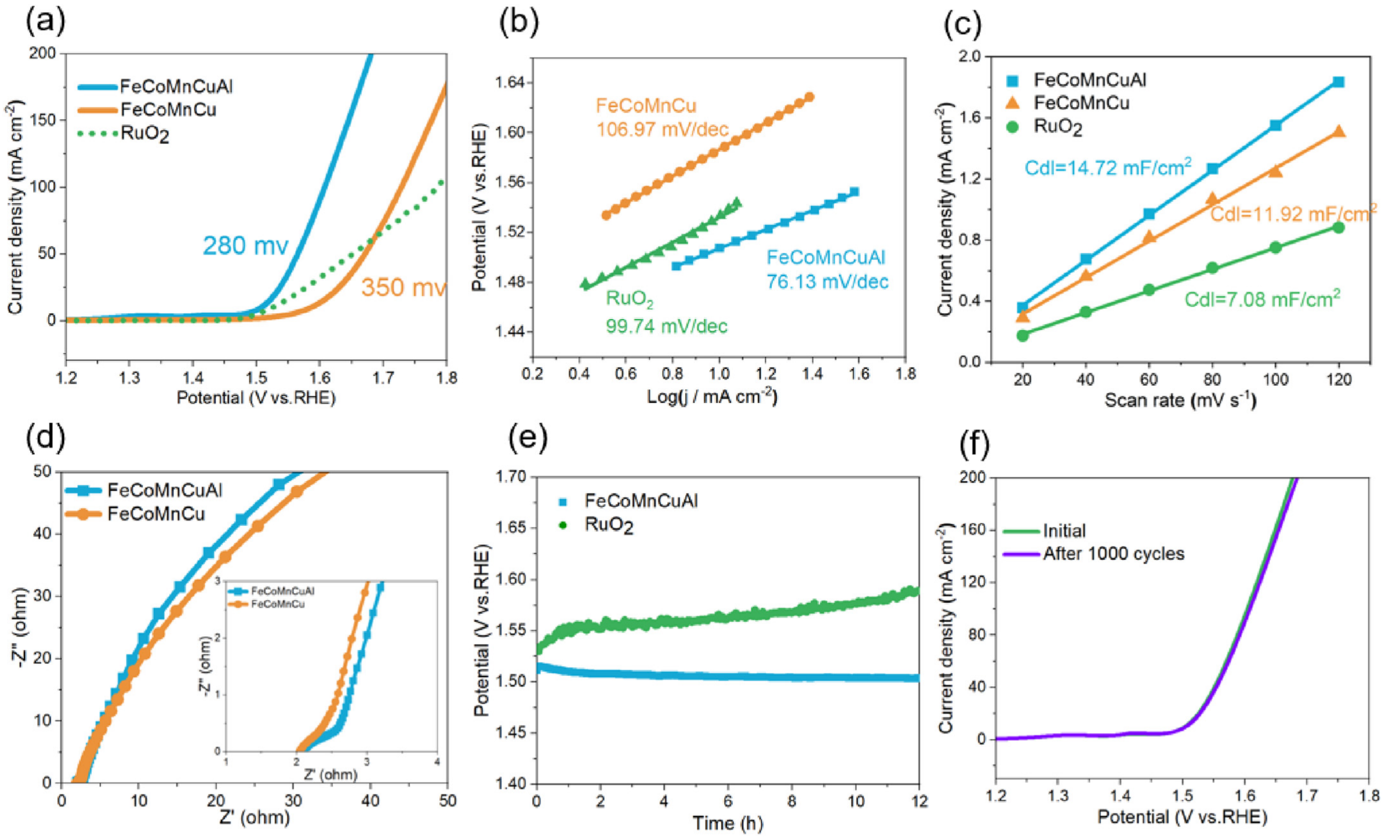

Fig. 4. (a) LSV curves, (b) Tafel slopes and (c) C_{dl} capacitances of FeCoMnCu, FeCoMnCuAl and commercial RuO_2 electrocatalysts. (d) EIS Nyquist plots of FeCoMnCu and FeCoMnCuAl electrocatalysts. (e) Long-term durability tests of FeCoMnCuAl and commercial RuO_2 electrocatalysts at 10 mA cm^{-2}. (f) LSV curves of FeCoMnCuAl electrocatalysts before and after 1000 cycles.

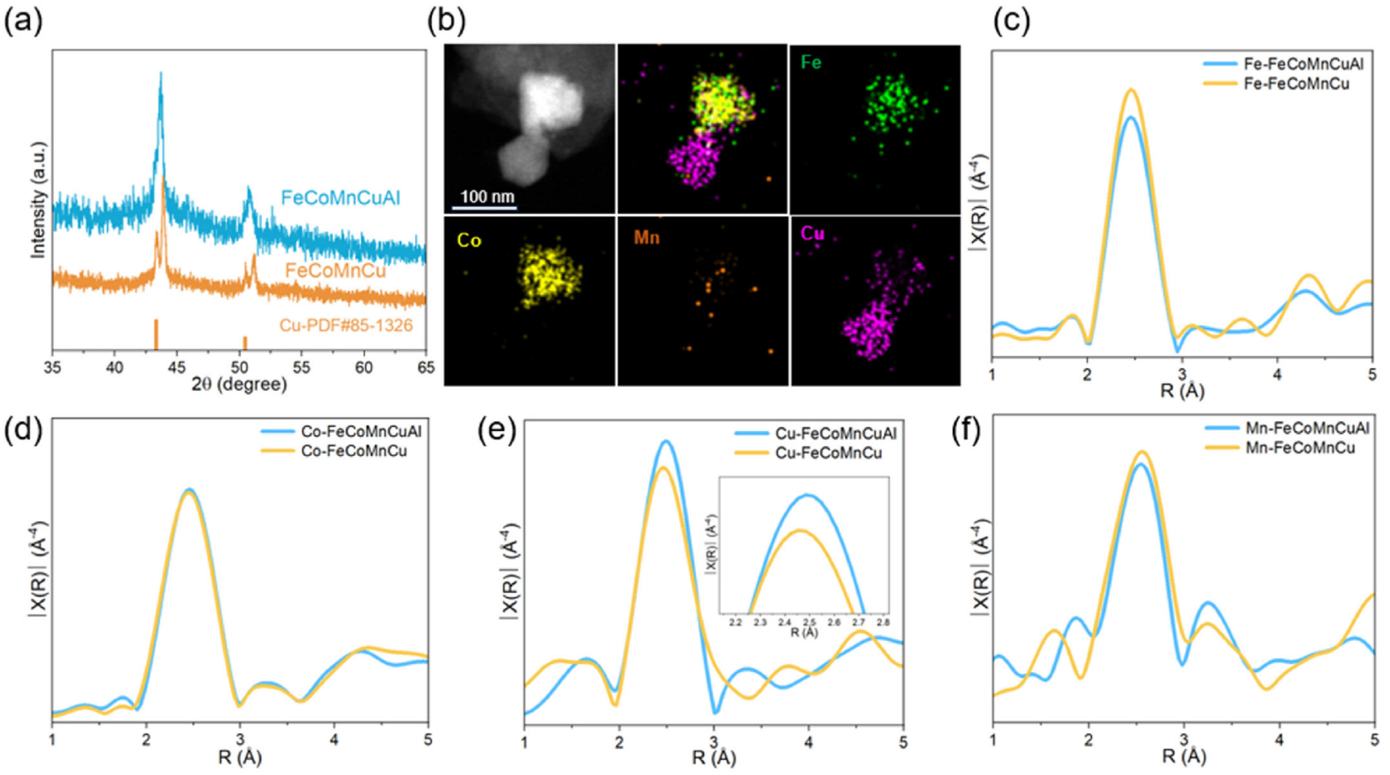

Fig. 5. (a) XRD patterns of FeCoMnCu and FeCoMnCuAl NPs. (b) EDS elemental mapping images of Fe, Co, Mn and Cu in FeCoMnCu NPs. The EXAFS spectra for (c) Fe, (d) Co, (e) Cu and (f) Mn k3-weighted K-edges.

the addition of Al element facilitates the formation of a single-phase solid solution. Fig. S5 presents the SEM images suggesting a relatively uniform size distribution in FeCoMnCu NPs, but the particle size is larger compared to that of FeCoMnCuAl. From TEM images, the size of FeCoMnCu particles is estimated to be around 50 nm (Fig. 5(b)). The EDS elemental mappings manifest two particles with different compositions, one containing only Cu and the another containing Fe, Co, Mn, and Cu (Fig. 5(b)), consistent with the XRD results. The Al element is more oxygen-friendly and accelerates the degradation of NPs due to the rapid formation of oxide layers [64], leading to smaller particle sizes and more active sites. Additionally, traditional transition metal electrocatalysts often suffer from low catalytic activity, easy oxidation, and difficult storage. The addition of Al element into electrocatalysts mitigates these issues, enhancing stability and preventing oxidation in the HEA electrocatalyst [65].

Fourier transforms of the phase-corrected EXAFS spectra (FT-EXAFS) confirm the absence of the $M - O$ shells (~1.9 Å) for $M = Fe, Co, Mn, Cu$ in both FeCoMnCuAl and FeCoMnCu electrocatalysts, validating their presence in metallic states. Meanwhile, the distance and amplitude of the first-shell M-M are almost identical for the Fe, Co, and Mn in both FeCoMnCuAl and FeCoMnCu electrocatalysts. However, the Cu-M bond length in the FeCoMnCuAl electrocatalyst is significantly longer than that in the FeCoMnCu electrocatalyst. This is due to the fact that phase separation of metallic Cu takes place in FeCoMnCu electrocatalyst, presenting shorter Cu–Cu bond lengths than other constituents (Fig. 5(c–f)). This observation is consistent with previous XRD and EDS results. Overall, the superior OER performance of FeCoMnCuAl HEA electrocatalyst may be attributed to the following factors: (a) the FeCoMnCuAl HEA electrocatalyst forms NPs with more adsorption sites which beneficials for electrocatalytic performance. (b) The FeCoMnCuAl electrocatalyst has unique structural that is different from the FeCoMnCu electrocatalyst by HTS method. (c) HTS method can achieve better interface stability between HEA NPs and substrates, so FeCoMnCuAl electrocatalyst have excellent stability performance in oxygen evolution reactions.

4. Conclusion

In this study, we prepared FeCoMnCuAl HEA NPs on several treated carbon substrates (cc, A-cc, H-cc, and AH-cc) *via* a HTS technique. These NPs were evaluated as cost-effective and efficient for the OER reaction. Comprehensive characterizations, including SEM, TEM, XRD, ICP, PDF, XPS, XAFS, etc., were performed to reveal the structural, compositional and electronic properties of the FeCoMnCuAl electrocatalyst. The FeCoMnCuAl electrocatalyst exhibits a low overpotential of 280 mV at a current density of 10 mA cm^{-2}, a Tafel slope of 76.13 mV dec^{-1} in 1 M KOH, and excellent stability without decay within 12 h, with significantly better performance than the precious metal RuO_2. This study provides a new approach for synthesizing nanoscale noble-metal-free HEA electrocatalysts for clean energy conversion applications on a large-scale basis for practical commercialization.

CRediT authorship contribution statement

Xindong Zhu: Writing – review & editing, Writing – original draft. **Wen Huang:** Writing – original draft. **Yu Lou:** Formal analysis. **Zhongzheng Yao:** Formal analysis. **Huiqiang Ying:** Formal analysis. **Min Dong:** Formal analysis. **Lan Tan:** Funding acquisition. **Jianrong Zeng:** Supervision. **Hua Ji:** Funding acquisition, Supervision. **He Zhu:** Writing – review & editing, Writing – original draft, Conceptualization. **Si Lan:** Supervision.

Declaration of competing interest

The authors declare that they have no known competing financial interests or personal relationships that could have appeared to influence the work reported in this paper.

Acknowledgements

This work was financially supported by the National Key R&D Program of China No. 2021YFB3802800, the National Natural Science Foundation of China (Grant Nos. 22275089, 52222104, 12261160364), the Fundamental Research Funds for the Central Universities (No. 30922010307). We thank the Shanghai synchrotron radiation facility (BL13SSW, SSRF) for help in experiments.

Appendix A. Supplementary data

Supplementary data to this article can be found online at https://doi.org/10.1016/j.pnsc.2024.08.005.

References

[1] P.Q. Liao, J.Q. Shen, J.P. Zhang, Metal-organic frameworks for electrocatalysis, Coord. Chem. Rev. 373 (2018) 22–48, https://doi.org/10.1016/j.ccr.2017.09.001.

[2] M.S. Faber, R. Dziedzic, M.A. Lukowski, N.S. Kaiser, Q. Ding, S. Jin, High-performance electrocatalysis using metallic cobalt pyrite (CoS_2) micro- and nanostructures, J. Am. Chem. Soc. 136 (28) (2014) 10053–10061, https://doi.org/10.1021/ja504099w.

[3] J. Yang, W. Li, D. Wang, Y. Li, Electronic metal-support interaction of single-atom catalysts and applications in electrocatalysis, Adv. Mater. 32 (49) (2020) 2003300, https://doi.org/10.1002/adma.202003300.

[4] X. Wang, J. Liu, Z. Liu, W. Wang, J. Luo, X. Han, et al., Identifying the key role of Pyridinic-N-Co bonding in synergistic electrocatalysis for reversible ORR/OER, Adv. Mater. 30 (23) (2018) 1800005, https://doi.org/10.1002/adma.201800005.

[5] B. Braunchweig, D. Hibbitts, M. Neurock, A. Wieckowski, Electrocatalysis: a direct alcohol fuel cell and surface science perspective, Catal. Today 202 (15) (2013) 197–209, https://doi.org/10.1016/j.cattod.2012.08.013.

[6] D.F. Du, S. Zhao, Z. Zhu, F.J. Li, J. Chen, Photo-excited oxygen reduction and oxygen evolution reactions enable a high-performance Zn-Air battery, Angew. Chem. 59 (41) (2020) 18140–18144, https://doi.org/10.1002/anie.202005929.

[7] G. Paul, S. Matthias, C. Matteo, A. Ricardo, N. Daniele, G. Leonardo, et al., The electron-proton bottleneck of photosynthetic oxygen evolution, Nature 617 (2023) 623–628, https://doi.org/10.1038/s41586-023-06008-5.

[8] H. Khani, N.S. Grundish, D.O. Wipf, J.B. Goodenough, Graphitic-shell encapsulation of metal electrocatalysts for oxygen evolution, oxygen reduction, and hydrogen evolution in alkaline solution, Adv. Energy Mater. 10 (1) (2020) 1903215, https://doi.org/10.1002/aenm.201903215.

[9] M. Cui, C. Yang, B. Li, Q. Dong, M. Wu, S. Hwang, et al., High-entropy metal sulfide nanoparticles promise high-performance oxygen evolution reaction, Adv. Energy Mater. 11 (3) (2021) 2002887, https://doi.org/10.1002/aenm.202002887.

[10] Y. Lu, K. Huang, X. Cao, L.Y. Zhang, T. Wang, D.D. Peng, et al., Atomically dispersed intrinsic hollow sites of M-M_1-M (M_1 = Pt, Ir; M = Fe, Co, Ni, Cu, Pt, Ir) on FeCoNiCuPtIr nanocrystals enabling rapid water redox, Advancrd Functional Materials 32 (19) (2022) 2110645, https://doi.org/10.1002/adfm.202110645.

[11] Y. Pi, J. Guo, Q. Shao, X. Huang, Highly efficient acidic oxygen evolution electrocatalysis enabled by porous Ir-Cu nanocrystals with three-dimensional electrocatalytic surfaces, Chem. Mater. 30 (23) (2018) 8571–8578, https://doi.org/10.1021/acs.chemmater.8b03620.

[12] M. Zhao, H. Li, W. Li, J. Li, L. Yi, W. Hu, et al., Ru-doping enhanced electrocatalysis of metal-organic framework nanosheets toward overall water splitting, Chemistry 26 (71) (2020) 17091–17096, https://doi.org/10.1002/chem.202002072.

[13] K. Tammeveski, J. Yu, Z. Chen, Non-precious-metal oxygen reduction reaction electrocatalysis, Chemelectrochem 5 (14) (2018) 1743–1744, https://doi.org/10.1002/celc.201800751.

[14] W.T. Hong, M. Risch, K.A. Stoerzinger, A. Grimaud, J. Suntivich, Y. Shao-Horn, Toward the rational design of non-precious transition metal oxides for oxygen electrocatalysis, Energy Environ. Sci. 8 (5) (2015) 1404–1427, https://doi.org/10.1039/C4EE03869J.

[15] A. Samanta, S. Das, S. Jana, Ultra-small intermetallic NiZn nanoparticles: a non-precious metal catalyst for efficient electrocatalysis, Nanoscale Adv. 2 (1) (2020) 417–424, https://doi.org/10.1039/c9na00611g.

[16] H. Sun, P. Zhou, Z. Tian, X. Ye, Z. Zhu, C. Ma, et al., Non-precious metal-doped carbon materials derived from porphyrin-based porous organic polymers for oxygen reduction electrocatalysis, ChemPlusChem 87 (7) (2022) 202200168, https://doi.org/10.1002/cplu.202200168.

[17] L.X. Liu, Y. Ding, L. Zhu, J.C. Li, H. Du, X. Li, et al., Recent advances in carbon-supported non-precious metal single-atom catalysts for energy conversion electrocatalysis, National Science Open 2 (2) (2023) 20220059, https://doi.org/10.1360/nso/20220059.

[18] H. Yu, L. Wu, B. Ni, T. Chen, Research progress on porous carbon-based non-precious metal electrocatalysts, Materials 16 (8) (2023) 3283, https://doi.org/10.3390/ma16083283.

[19] C.W. Lu, Y.S. Lu, Z.H. Lai, H.W. Yen, Y.L. Lee, Comparative corrosion behavior of $Fe_{50}Mn_{30}Co_{10}Cr_{10}$ dual-phase high-entropy alloy and CoCrFeMnNi high-entropy

alloy in 3.5 wt% NaCl solution, J. Alloys Compd. 842 (2020) 155824, https://doi.org/10.1016/j.jallcom.2020.155824.

[20] Z.Q. Chen, J.B. Wen, C.H. Wang, X.W. Kang, Convex cube-shaped $Pt_{34}Fe_5Ni_{20}Cu_{31}Mo_9Ru$ high entropy alloy catalysts toward high-performance multifunctional electrocatalysis, Small 18 (45) (2022) 2204255, https://doi.org/10.1002/smll.202204255.

[21] J. Chen, X. Zhou, W. Wang, B. Liu, Y. Lv, W. Yang, et al., A review on fundamental of high entropy alloys with promising high-temperature properties, J. Alloys Compd. 760 (2018) 15–30, https://doi.org/10.1016/j.jallcom.2018.05.067.

[22] D. Karlsson, A. Marshal, F. Johansson, M. Schuisky, M. Sahlberg, J.M. Schneider, U. Jansson, Elemental segregation in an AlCoCrFeNi high-entropy alloy – a comparison between selective laser melting and induction melting, J. Alloys Compd. 784 (2019) 195–203, https://doi.org/10.1016/j.jallcom.2018.12.267.

[23] X.R. Huo, X.J. Zuo, X. Wang, B.W. Xing, N.N. Zhang, High entropy alloy CoCrFeNiMo reinforced electrocatalytic performance for high-efficient electrocatalytic water splitting, Chemistry 18 (15) (2023) e202300456, https://doi.org/10.1002/asia.202300456.

[24] C. Ng, S. Guo, J. Luan, S. Shi, C.T. Liu, Entropy-driven phase stability and slow diffusion kinetics in an $Al_{0.5}CoCrCuFeNi$ high entropy alloy, Intermetallics 31 (2012) 165–172, https://doi.org/10.1016/j.intermet.2012.07.001.

[25] X. Liu, Y. Duan, X. Yang, L. Huang, M. Gao, T. Wang, Enhancement of magnetic properties in $FeCoNiCr_{0.4}Cu_X$ high entropy alloys through the cocktail effect for megahertz electromagnetic wave absorption, J. Alloys Compd. 872 (2021) 159602, https://doi.org/10.1016/j.jallcom.2021.159602.

[26] Y.Z. Zhou, K.H. Huang, G.X. Bo, S.C. Luo, W.M. Guo, S.K. Sun, H.T. Lin, Synergistic effects of high-entropy alloy addition on hardness and fracture toughness of (Ti, Nb, Ta, Mo, W) (C, N)-based high-entropy ceramics, Ceram. Int. 49 (21) (2023) 33652–33658, https://doi.org/10.1016/j.ceramint.2023.08.047.

[27] Y.H. Wang, L. Li, J. H Shi, M.Y. Xie, J.H. Nie, G.F. Huang, et al., Oxygen defect engineering promotes synergy between adsorbate evolution and single lattice oxygen mechanisms of OER in transition metal-based (oxy)hydroxide, Adv. Sci. 10 (32) (2023) 2303321, https://doi.org/10.1002/advs.202303321.

[28] Y. Yang, Z. Jia, X. Zhang, Y. Liu, Q. Wang, Y. Li, et al., Chemical short-range order in multi-principal element alloy with ordering effects on water electrolysis performance, Mater. Today 72 (2024) 112–123, https://doi.org/10.1016/j.mattod.2023.12.006.

[29] Z. Li, K.G. Pradeep, Y. Deng, D. Raabe, C.C. Tasan, Metastable high-entropy dual-phase alloys overcome the strength-ductility trade-off, Nature 534 (7606) (2016) 227–230, https://doi.org/10.1038/nature17981.

[30] W. Shi, H. Liu, Z. Li, C. Li, J. Zhou, Y. Yuan, et al., High-entropy alloy stabilized and activated Pt clusters for highly efficient electrocatalysis, SusMat 2 (2) (2022) 186–196, https://doi.org/10.1002/sus2.56.

[31] H.H. Kristoffersen, J. Rossmeisl, Local order in AgAuCuPdPt high-entropy alloy surfaces, J. Phys. Chem. C 126 (15) (2022) 6782–6790, https://doi.org/10.1021/acs.jpcc.2c00478.

[32] Q. Zhang, K. Lian, Q. Liu, G. Qi, S. Zhang, J. Luo, X. Liu, High entropy alloy nanoparticles as efficient catalysts for alkaline overall seawater splitting and Zn-air batteries, J. Colloid Interface Sci. 646 (2023) 844–854, https://doi.org/10.1016/j.jcis.2023.05.074.

[33] K. Zeng, J. Zhang, W. Gao, L. Wu, H. Liu, J. Gao, et al., Surface-decorated high-entropy alloy catalysts with significantly boosted activity and stability, Adv. Funct. Mater. 32 (33) (2022) 2204643, https://doi.org/10.1002/adfm.202204643.

[34] Y. Yang, Z. Jia, Q. Wang, Y. Liu, L. Sun, B. Sun, et al., Vacancy induced microstrain in high-entropy alloy film for sustainable hydrogen production under universal pH conditions, Energy Environ. Sci. (2024), https://doi.org/10.1039/d4ee01139b.

[35] X. Zhang, Y. Yang, Y. Liu, Z. Jia, Q. Wang, L. Sun, et al., Defect engineering of a high-entropy metallic glass surface for high-performance overall water splitting at ampere-level current densities, Adv. Mater. 35 (38) (2023) 2303439, https://doi.org/10.1002/adma.202303439.

[36] X.C. Zhou, S.Q. Chen, M.J. Zhou, M. Li, S. Lan, T. Feng, Highly efficient cobalt-based amorphous catalyst for peroxymonosulfate activation toward wastewater remediation, Rare Met. 42 (4) (2023) 1160–1174, https://doi.org/10.1007/s12598-022-02220-w.

[37] L. Zhan, Z. Han, Q. Shao, M.L. Etheridge, T. Hays, J.C. Bischof, Rapid joule heating improves vitrification-based cryopreservation, Nat. Commun. 13 (1) (2022) 6017, https://doi.org/10.1038/s41467-022-33546-9.

[38] Y.T. Liao, R.T. Zhu, W.J. Zhang, H.Y. Zhu, Y. Sun, J.L. Chen, et al., Transient synthesis of carbon-supported high-entropy alloy sulfide nanoparticles via flash joule heating for efficient electrocatalytic hydrogen evolution, Nano Res. 17 (4) (2024) 3379–3389, https://doi.org/10.1007/s12274-023-6215-8.

[39] Y.X. Wang, Y. Zhang, P.Y. Xing, X.Q. Li, Q.Y. Du, X.Q. Fan, et al., Self-encapsulation of high-entropy alloy nanoparticles inside carbonized wood for highly durable electrocatalysis, Adv. Mater. 36 (28) (2024) 2402391, https://doi.org/10.1002/adma.202402391.

[40] X.X. Zou, J.Y. Xie, Z.Y. Mei, Q. Jing, X.L. Sheng, C.H. Zhang, et al., High-entropy engineering with regulated defect structure and electron interaction tuning active sites for trifunctional electrocatalysis, Proc. Natl. Acad. Sci. U.S.A. 121 (13) (2024) e2313239121, https://doi.org/10.1073/pnas.2313239121.

[41] J.H. Cha, S.H. Cho, D.H. Kim, D.Y. Jeon, S. Park, J.W. Jung, et al., Flash-thermal shock synthesis of high-entropy alloys toward high-performance water splitting, Adv. Mater. 35 (46) (2023) 2305222, https://doi.org/10.1002/adma.202305222.

[42] B. Deng, Z. Wang, W. Chen, J.T. Li, D.X. Luong, R.A. Carter, et al., Phase controlled synthesis of transition metal carbide nanocrystals by ultrafast flash Joule heating, Nat. Commun. 13 (1) (2022) 262, https://doi.org/10.1038/s41467-021-27878-1.

[43] Y. Yao, Z. Huang, P. Xie, S.D. Lacey, R.J. Jacob, H. Xie, et al., Carbothermal shock synthesis of high-entropy-alloy nanoparticles, Science 359 (6383) (2018) 1489–1494, https://doi.org/10.1126/science.aan5412.

[44] Y.Z. Liu, X.B. Hu, S.J. Geng, Y.L. Zhu, H. Wei, X.L. Ma, Microstructural evolution of the interface between NiCrAlY coating and superalloy during isothermal oxidation, Mater. Des. 80 (2015) 63–69, https://doi.org/10.1016/j.matdes.2015.05.014.

[45] J. Kim, H. Choi, D. Kim, J.Y. Park, Operando surface studies on metal-oxide interfaces of bimetal and mixed catalysts, ACS Catal. 11 (14) (2021) 8645–8677, https://doi.org/10.1021/acscatal.1c02340.

[46] M.C. Luo, Z.L. Zhao, Y.L. Zhang, Y.J. Sun, Y. Xing, F. Lv, et al., PdMo bimetallene for oxygen reduction catalysis, Nature 574 (2019) 81–85, https://doi.org/10.1038/s41586-019-1603-7.

[47] X. Qiu, J.W. Thompson, S.J.L. Billinge, PDFgetX2: a GUI-driven program to obtain the pair distribution function from X-ray powder diffraction data, J. Appl. Crystallogr. 37 (2004) 678, https://doi.org/10.1107/S0021889804011744.

[48] B. Ravel, M. Newville, ATHENA, artemis, hephaestus: data analysis for X-ray absorption spectroscopy using IFEFFIT, J. Synchrotron Radiat. 12 (2005) 537–541, https://doi.org/10.1107/S0909049505012719.

[49] A.J. Ramiro de Castro, G.D. Saraiva, A.C. Oliveira, V.O. Sousa Neto, A.J. Paula, A.G. Souza Filho, et al., Ordered porous carbons from hydrothermally treated biomass: effects of the thermal treatments on the structure and porosity, Vib. Spectrosc. 111 (2020) 103175, https://doi.org/10.1016/j.vibspec.2020.103175.

[50] J. Hu, T.Q. Guo, X.Y. Zhong, J. Li, Y.J. Mei, C.X. Zhang, et al., In situ reconstruction of high-entropy heterostructure catalysts for stable oxygen evolution electrocatalysis under industrial conditions, Adv. Mater. 36 (2024) 2310918, https://doi.org/10.1002/adma.202310918.

[51] Y. Yao, Z. Huang, P. Xie, S.D. Lacey, R.J. Jacob, H. Xie, et al., Carbothermal shock synthesis of high-entropy-alloy nanoparticles, Science 359 (2018) 1489–1494, https://doi.org/10.1126/science.aan5412.

[52] M. Jin, L. Cheng, W. Zheng, Y. Ding, Y.M. Zhu, L.M. Jia, et al., Raman tensor of graphite: symmetry of G, D and D′ phonons, Sci. China Mater. 65 (2022) 268–272, https://doi.org/10.1007/s40843-021-1741-0.

[53] Y.C. Liu, X.L. Tian, Y.C. Han, Y.N. Chen, W.B. Hu, High-temperature shock synthesis of high-entropy-alloy nanoparticles for catalysis, Chin. J. Catal. 48 (2023) 66–89, https://doi.org/10.1016/S1872-2067(23)64428-6.

[54] L. Zhu, X.Y. Li, X.Z. Feng, X.Y. Li, X.Y. Xu, Synthesis and characterization of mesoporous graphite carbon, and adsorption performance for benzene, J. Porous Mater. 23 (2016) 957–965, https://doi.org/10.1007/s10934-016-0153-8.

[55] S.H. Chang, Y.T. Tsao, K.W. Tung, Heat treatment effect on the surface properties of carbon cloth electrode for microbial fuel cell, Mater. Sci. 27 (3) (2021) 361–366, https://doi.org/10.5755/j02.ms.27630.

[56] C.J. Zhao, W.L. Cai, N. Sun, S. Chen, W.B. Jing, C.H. Zhao, Facile preparation of porous high-entropy alloy FeCoNiCuMn and its OER performance, J. Phys. Chem. Solid. 184 (2024) 111668, https://doi.org/10.1016/j.jpcs.2023.111668.

[57] J.H. Zhao, Z.Y. Wang, X.Y. Fang, L. Yang, C.Q. Wu, W. Gan, et al., Fast joule heating synthesis of NiCoFeCrMo high-entropy alloy embedded in graphene for water oxidation, J. Alloys Compd. 966 (2023) 171535, https://doi.org/10.1016/j.jallcom.2023.171535.

[58] L. Li, X. Cao, J. Huo, J. Qu, W. Chen, C. Liu, High valence metals engineering strategies of Fe/Co/Ni-based catalysts for boosted OER electrocatalysis, J. Energy Chem. 76 (2023) 195–231, https://doi.org/10.1016/j.jechem.2022.09.022.

[59] N.T. Suen, S.F. Hung, Q. Quan, N. Zhang, Y.J. Xu, H.M. Chen, Electrocatalysis for the oxygen evolution reaction: recent development and future perspectives, Chem. Soc. Rev. 46 (2) (2017) 337–365, https://doi.org/10.1039/c6cs00328a.

[60] T.Q. Guo, L.D. Li, Z.C. Wang, Recent development and future perspectives of amorphous transition metal-based electrocatalysts for oxygen evolution reaction, Adv. Energy Mater. 12 (24) (2022) 2200827, https://doi.org/10.1002/aenm.202200827.

[61] Z.Y. Jin, J. Lv, H.L. Jia, W.H. Liu, H.L. Li, Z.H. Chen, et al., Nanoporous Al-Ni-Co-Ir-Mo high-entropy alloy for record-high water splitting activity in acidic environments, Small 15 (47) (2019) 1904180, https://doi.org/10.1002/smll.201904180.

[62] P. Yang, Y.P. An, C.R. Feng, Y.X. Liu, S.B. Liu, L.Q. Gao, et al., Heterogeneous high-entropy catalyst nanoparticles for oxygen evolution reaction: impact of oxygen and fluorine introduction, Int. J. Hydrogen Energy 51 (2024) 1218–1228, https://doi.org/10.1016/j.ijhydene.2023.09.143.

[63] X. Xu, H. Zhu, Y. Tang, L.G. Wang, Q.H. Zhang, Y. Ren, et al., Spreading monoclinic boundary network between hexagonal primary grains for high performance Ni-rich cathode materials, Nano Energy 100 (2022) 107502, https://doi.org/10.1016/j.nanoen.2022.107502.

[64] T. Reier, M. Oezaslan, P. Strasser, Electrocatalytic oxygen evolution reaction (OER) on Ru, Ir, and Pt Catalysts: a comparative study of nanoparticles and bulk materials, ACS Catal. 2 (8) (2012) 1765–1772, https://doi.org/10.1021/cs3003098.

[65] S. Miller, C. Dsilva, J.R. Kitchin, Coverage dependent adsorption properties of atomic adsorbates on late transition metal surfaces, Catalysis 24 (2012) 83–115, https://doi.org/10.1039/9781849734776-00083.